

# Effects of baryons on the gravitational redshift profile of $\Lambda$ CDM halos

Hongyu Zhu<sup>1,2\*</sup>, Shadab Alam<sup>3,1,2</sup>, Rupert A. C. Croft<sup>1,2,4</sup>, Shirley Ho<sup>1,2,5,6,7</sup>, Elena Giusarma<sup>1,2,5,6</sup>

<sup>1</sup> *Department of Physics, Carnegie Mellon University, 5000 Forbes Ave., Pittsburgh, PA 15213*

<sup>2</sup> *McWilliams Center for Cosmology, Carnegie Mellon University, 5000 Forbes Ave., Pittsburgh, PA 15213*

<sup>3</sup> *Institute for Astronomy, University of Edinburgh, Royal Observatory, Blackford Hill, Edinburgh, EH9 3HJ, UK*

<sup>4</sup> *ASTRO-3D Center, School of Physics, University of Melbourne, Parkville, VIC 3010, Australia*

<sup>5</sup> *Berkeley Center for Cosmological Physics, University of California, Berkeley, CA 94720, USA*

<sup>6</sup> *Lawrence Berkeley National Laboratory (LBNL), Physics Division, Berkeley, CA 94720, USA*

<sup>7</sup> *Flatiron Institute, Center for Computational Astrophysics, 162 Fifth Ave., New York, NY, USA 10010*

11 March 2024

## ABSTRACT

Gravitational redshifts and other relativistic effects are beginning to be studied in the context of galaxy clustering. Distortions consistent with those expected in General Relativity have been measured in galaxy cluster redshift profiles by Wojtak et al. and others and in the cross-correlation function of galaxy populations by Alam et al. On scales below  $\sim 20$  Mpc/ $h$  simulations have shown that gravitational redshift dominates over other effects. However, this signal is related to the shape and depth of gravitational potentials, and therefore the matter density in galaxies and galaxy clusters that is responsible for them. We investigate the effects of baryonic physics on the gravitational redshift profiles of massive (group and cluster-sized) halos. We compare the profiles of different components in halos taken from the MassiveBlack-II cosmological hydrodynamic simulation and a dark matter-only version of the same simulation. We find that inclusion of baryons, cooling, star formation and feedback significantly alters the relevant inner density profiles. These baryonic effects lead to overall increases in both gravitational redshifts and the transverse relativistic Doppler effects by up to  $\sim 50\%$  for group size halos. We show how modified Navarro Frenk White halo profiles can be used to parametrize these differences, and provide relevant halo profile fits.

**Key words:** hydrodynamical simulation; gravity

## 1 INTRODUCTION

The structure of Universe is thought to have formed from the growing modes of tiny quantum fluctuations in an initial homogeneous field. Such growing modes collapsed through gravity and formed what we call today dark matter halos. These dark matter halos provided the necessary environment for baryonic component of the matter to collapse further and form stars at the smallest level and larger structures like galaxies, collections of stars held together in gravitationally nurturing environment of dark matter halos. The baryonic component's evolution through several highly energetic events of star and galaxy formation also shapes the dark matter itself especially in the innermost regions. All such effects taken together in the structure formation paradigm are

known as baryonic effects on dark matter halos. These become extremely important for studies which are sensitive to the innermost parts of the halos for example gravitational lensing (Dodelson 2003; Zentner et al. 2013; Huang et al. 2018), SZ effects, galaxy velocity bias, and gravitational redshift.

Several attempts have been made to understand and predict the nature of the inner structures of dark matter halos. Navarro et al. (1996, 1997) showed that density profiles of simulated dark matter halos have all the same shape, independent of the halo mass, the initial density fluctuation spectrum, and the values of the cosmological parameters, by studying the equilibrium density profiles of dark matter halos from  $N$ -body models. The NFW density profile can be

\* E-mail: hongyuz@andrew.cmu.edu

expressed with the simple formula

$$\rho(r) = \frac{\rho_{\text{crit}}(z)\delta_c}{(r/r_s)(1+r/r_s)^2}, \delta_c = \frac{200}{3} \frac{c^3}{\ln(1+c) - c/(1+c)} \quad (1)$$

where  $\rho_{\text{crit}}(z) = 3H^2(z)/8\pi G$  is the critical density at redshift  $z$ ,  $r_s$  is the scale radius and  $\delta_c$  is a characteristic (dimensionless) density.  $c = R_{200}/r_s$  is the “concentration” of the halo that provides a link between  $r_s$  and  $\delta_c$ . Navarro et al. (1997) also found that massive halos are less concentrated than smaller halos. The very inner slope in Eqn. 1,  $d \ln \rho(r)/d \ln r|_{r \rightarrow 0} = -1$ . This inner slope is difficult to measure, and very sensitive to baryonic physics, something which was not modelled in the initial dark matter halo studies. For instance, Moore et al. (1999) used a profile with a steeper inner slope -1.5. A generalized NFW (hereafter gNFW) density profile (e.g. Hernquist 1990; Zhao 1996) was proposed, being:

$$\rho(r) = \frac{\rho_{\text{crit}}(z)\delta_c}{(r/r_s)^\gamma (1+r/r_s)^{3-\gamma}}. \quad (2)$$

In Eqn. 2,  $d \ln \rho(r)/d \ln r|_{r \rightarrow 0} = -\gamma$  is an additional free parameter (e.g. Schmidt & Allen 2007). Navarro et al. (2004) also explored a more general model, similar to that of de Vaucouleurs (de Vaucouleurs 1948) in which the logarithmic slope varies continuously with radius. This model happened to be the same as one introduced by Jaan Einasto at a 1963 conference in Alma-Ata, Kazakhstan (Einasto 1965). It is therefore referred to as “Einasto’s model”. Einasto’s model is expressed as

$$\rho(r) = \rho_{-2} \exp \left\{ -\frac{2}{\alpha} \left[ \left( \frac{r}{r_{-2}} \right)^\alpha - 1 \right] \right\}. \quad (3)$$

As pointed out by Merritt et al. (2005), Einasto’s model has the same slope-radius relation as Sersic’s model (Sérsic 1963) and works well for both projected (surface) density and (space) density profiles of galaxies. Eqn. 3 can be also written as  $d \ln \rho(r)/d \ln r = -2(r/r_{-2})^\alpha$  where  $r_{-2}$  is the radius that yields a  $\rho(r)$  slope in log-log space of  $-2$ , with  $\rho_{-2}$  the density at that radius. It can be seen that Einasto’s model is a generalization of a power law in log-log space and that the parameter  $\alpha$  controls curvature of the profile. Einasto’s model has been used to describe many types of system including galaxies and dark matter halos and it is often considered a better fit than the NFW model to  $N$ -body dark matter halo profiles (Merritt et al. 2006).

Baryonic effects such as radiative cooling and feedback have been investigated in a variety of simulations such as the Overwhelmingly Large Simulations project (OWLS), Feedback In Realistic Environments (FIRE), Millennium Simulation (MS), Evolution and Assembly of Galaxies and their Environment (EAGLE) (Neto et al. 2007; Rudd et al. 2008; Duffy et al. 2010; Velliscig et al. 2014; Chan et al. 2015; Schaller et al. 2015a,b). It has been claimed that simulated dark matter profiles would be steeper in the inner regions than the NFW profile if the cooling is efficient and feedback is weak since the gravity of the central baryons pulls dark matter towards the center; without this, dark matter profiles would be shallower. The slope of the inner dark matter density profile therefore shows a strong mass dependence. To understand the structure of the inner halo is crucial as it is not only of major importance for efforts to detect dark matter experimentally but also central to possible issues which

have been identified with the  $\Lambda$ CDM paradigm from small scales, such as the *cusp/core* problem (de Blok 2010).

Gravitational redshift is one of the major predicted effects that occur in weak gravitational fields according to the principle of equivalence from General relativity (Einstein 1916). A photon with wavelength  $\lambda$  emitted in a gravitational potential  $\Phi$  and observed at infinity has a gravitational redshift  $z_g = \Delta\lambda/\lambda \approx \Delta\Phi/c^2$ . The effect has been measured for the Earth’s gravity, in the Solar system and in white dwarf stars (e.g. Pound & Rebka 1959; Takeda & Ueno 2012; Falcon et al. 2010) as one of the fundamental tests of General relativity. By assuming an analytic de Vaucouleurs profile, Cappi (1995) argued that gravitational redshifts of central galaxies in clusters with respect to the other cluster members would be tens of km/s in the most massive galaxy clusters, which is feasible to detect. Kim & Croft (2004) used  $N$ -body simulations to show that it should be possible to detect the radial profile of gravitational redshifts in galaxy clusters. Wojtak et al. (2011) carried out the first observational measurement of gravitational redshifts in galaxy clusters and found consistency with General relativity.

Croft (2013) predicted a  $\sim 4\sigma$  signal of gravitational redshifts from large-scale structure should be obtainable from the full Baryonic Oscillation Spectroscopic Survey (BOSS) by examining the distortion due to gravitational redshifts of the cross-correlation function of two galaxy populations. The relativistic distortions cause a dipole in clustering which is not present when they are not included (McDonald 2009). Besides the gravitational redshift effect, there exist other relativistic effects comparable in magnitude such as the transverse Doppler effect, light cone bias and special relativistic beaming, as pointed out by Kaiser (2013) and Giusarma et al. (2016), and modeled in simulations by Zhao et al. (2013), Cai et al. (2017), Alam et al. (2017b) and Zhu et al. (2017). These were included in comparisons to an observational measurement of relativistic distortions in galaxy clustering Alam et al. (2017a). These effects are included to linear order in the GR perturbation theory treatments of (Yoo et al. 2009, 2012; Bonvin et al. 2014). Most relevant to the current paper is the fact that Zhu et al. (2017), and Breton et al. (2018) find that gravitational redshift dominates the non-linear regime, and consequently the range of scales where signal to noise of measurements is largest. Here the resolution of  $N$ -body simulations and the clustering of baryons on small scales are crucial for measuring and understanding relativistic effects.

In this paper we use the MassiveBlack-II (hereafter MBII) high resolution hydrodynamical simulation (Khandai et al. 2015) to predict the effects of baryonic physics on the gravitational redshift of galaxies. We also compare to a dark matter-only simulation (hereafter DMO) run with the same volume, cosmological parameters, and initial conditions (Tenneti et al. 2015). Comparing the outputs from these two enables us to study the baryonic effects in dark matter halos.

This paper examines the small scale behavior of gravitational redshift profiles in and around galaxies as well as the effects of baryons on small scales. Our plan for the paper is as follows. We discuss the simulations we used, the approach to the sample and how we obtain the gravitational potential from MBII and its corresponding dark matter-only

simulations in Sec. 2. In Sec. 3.1 we show the density and gravitational profiles of massive halos from different components and simulations. The comparison between simulation (spatial) and observational (projected) quantities is explored in the last part of Sec. 3.1. In Sec. 4, we fit analytic models to the profiles, demonstrating the effects of baryons in a more quantitative way. Sec. 5 presents another comparable relativistic effect, the transverse Doppler effect and explores how baryonic physics affects it. We conclude in Sec. 6 with a summary and a discussion of our findings.

## 2 SIMULATIONS

The hydrodynamic simulation we use, MBII (Khandai et al. 2015) was run using P-GADGET, a massively parallel TreeSPH cosmological simulation code combining a collisionless fluid with the  $N$ -body method and an ideal gas by means of smoothed particle hydrodynamics (SPH) (see Springel 2005 for a predecessor public version, GADGET-2). The cosmological parameters in MBII and DMO simulation are  $\sigma_8 = 0.816$ ,  $n_s = 0.968$ ,  $\Omega_\lambda = 0.725$ ,  $\Omega_m = 0.275$ ,  $\Omega_b = 0.046$  (MBII) and  $h = 0.071$ . Simulation parameters are listed in Tbl. 1. MBII is large enough to contain massive halos of mass above  $10^{14} M_\odot/h$  as the cubical comoving volume is  $(100 \text{ Mpc}/h)^3$  (Khandai et al. 2015). MBII includes the models for star formation, black hole (BH) growth and radiative cooling and heating processes. Such massive halos are expected to show a  $\sim 10 \text{ km/s}$  difference in gravitational redshift between their centers and edges. Furthermore, a corresponding dark matter-only simulation to MBII was performed with the same volume, cosmological parameters, and initial conditions (Tenneti et al. 2015). Comparing the results from these two enables us to study the impact of baryonic processes on the properties of dark matter halos.

### 2.1 Halos and subhalos

As described in (Khandai et al. 2015; Tenneti et al. 2015), the halos are identified through the friends-of-friends (FOF) algorithms (Davis et al. 1985) on dark matter particles with a linking length of  $b = 0.2$  times the mean of particle separations. Gas and stars are associated to their closest dark matter particles. SUBFIND code (Springel et al. 2001) is used to find subhalos which are locally overdense, self-bound groups of particles within halos. The process starts with isolated local density peaks inside halos and expands until the overdensity reaches a certain threshold.

**Table 1.** Simulation parameters in MBII and DMO:  $N_{\text{part}}$ ,  $m_{\text{DM}}$ ,  $m_{\text{gas}}$  and  $\epsilon = 1.85 \text{ kpc}/h$

	$N_{\text{part}}$	$m_{\text{DM}} [M_\odot/h]$	$m_{\text{gas}} [M_\odot/h]$
MBII	$2 \times 1792^3$	$1.1 \times 10^7$	$2.2 \times 10^6$
DMO	$1792^3$	$1.32 \times 10^7$	NA

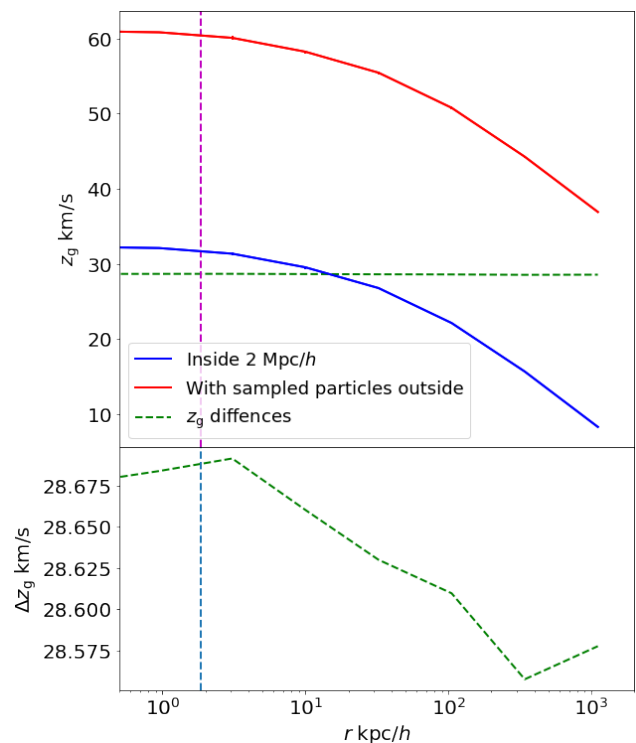


**Figure 1.** A test of the gravitational redshift calculation: The gravitational redshift profiles of particles within  $2 \text{ Mpc}/h$  (blue), of both inside particles and sampled  $N_{\text{sample}}$  particles outside (red) and their difference (green) in the MBII simulation in the halo of mass  $> 7 \times 10^{14} M_\odot/h$ . The center is chosen at the potential minimum in the halo. The bottom panel magnifies the difference (green) between red and blue lines in the top panel.

### 2.2 Efficient Calculation of gravitational redshift potential

Generally cosmological simulations produce a massive amount of data which are difficult to store with limited disk space. Traditionally the gravitational potential of particles are not stored as it is not needed for standard analysis. We therefore devise a method to obtain the potentials for each particle in the simulation in post-processing. Given enough resources, the simplest method to obtain the potential is to use the same  $N$ -body code initially used to produce the simulations, loading all the particles and velocities and running for a single time step with instruction to also save the calculated potential. However, since only the potentials for the particles within selected halos are needed, and local computing resources are not able to run the full 11.5 billion particle MBII hydro simulation, we use an alternative technique. We select all particles within  $2 \text{ Mpc}/h$  of the halo centres since we are only interested in the gravitational redshift profile on small scales, and also randomly sample  $N_{\text{sample}} = 2,000,000$  particles outside this range. For the sparse sample particles, we multiply the mass of sampling particles by a factor of  $N_{\text{outside}}/N_{\text{sample}}$  where  $N_{\text{outside}}$  denotes the total number of particles outside  $2 \text{ Mpc}/h$ . We calculate gravitational redshift profiles both with and without the sampled  $N_{\text{sample}}$  particles outside and compute the difference between them (See Fig. 1). The gravitational redshift profiles are quite

smooth and the difference is a constant as expected, though with  $<1\%$  fluctuations that are barely visible. Therefore, in our further discussions about gravitational redshifts, we only use the particles inside the  $2 \text{ Mpc}/h$  radius since a constant in  $z_g$  (i.e. potential) can be considered the same as assigning a different zero-point potential which makes no difference to the physics.

### 3 DENSITY AND GRAVITATIONAL PROFILES OF MASSIVE HALOS

The dark matter haloes and galaxies live in three spatial dimensions but in observations we are always limited to projected profile in the plane of sky. Therefore it is important to distinguish the two and understand the impact of projection on the measurement. In the following sections we discuss both three dimensional spatial profiles and projected profiles while contrasting the two with each other.

#### 3.1 Spatial (deprojected) profiles

We concentrate on the most massive halo at  $z = 0.06$  in the MBII hydrodynamical simulation (MBII) and its equivalent in MBII dark matter-only (DMO) simulation. The halo has a mass  $7 \times 10^{14} M_\odot/h$  and most of that mass is in a large subhalo of mass  $6 \times 10^{14} M_\odot/h$ . There are slight differences in mass and positions of the halo between the two simulations. The profiles are calculated using the potential minima of this halo as the center and the small offset between MBII and DMO is accounted for. We first want to understand the scale dependence of dark matter density and which parts of halos are dominated by different components. We show the angular averaged density profile from the center of halos in Figure 2. It can be seen that the distributions of total matter in the DMO and MBII simulations are nearly identical on large scales, showing that baryonic effects are negligible beyond  $0.1 r_{200}$ . For MBII, dark matter is the major component for radii larger than  $\sim 0.005 R_{200}$ . Stellar matter is the dominant component for the inner radii (below  $\sim 0.005 R_{200}$ ) and exhibits a steeper profile within this radius. The gas is concentrated near the center and becomes negligible at radii larger than  $\sim 0.005 R_{200}$ . For DMO, the dark matter profile is much flatter close to the center compared to the dark matter profile in MBII, lacking the contraction caused by the gravity of a core of stars and dense cooling gas.

Fig. 3 shows the contributions from gas, dark matter and stars to the gravitational redshift profile of the same halo. The differences between the center and edges are of the order of  $\sim 10 \text{ km/s}$  as expected. Gas and stellar mass contribute  $\sim 1$  order of magnitude less than dark matter because dark matter is similarly less abundant in mass. Though stellar mass is more concentrated in the center, it quickly becomes sparser at distances larger than  $\sim 0.005 R_{200}$ . As a result, it still makes the smallest contribution to the gravitational redshift around the center and its contribution decays rapidly with increasing radius. We can also see in Fig. 3 that the existence of baryons steepens the gravitational redshift profile as the dark matter has been pulled inward during cooling. We also investigate other 8 massive halos and find there is in all cases a 20% - 50%

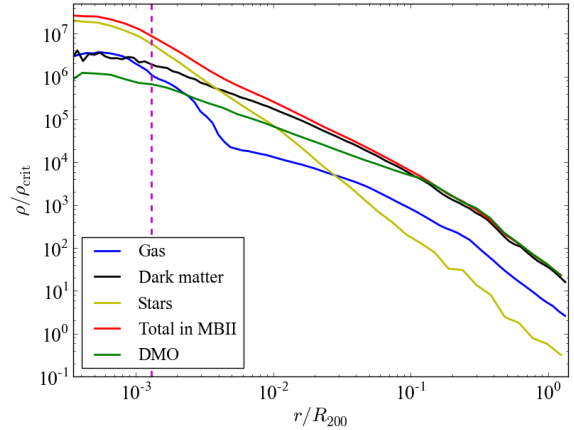


**Figure 2.** The density profiles of gas (blue), dark matter (black), stars (yellow) and total matter (red) in MBII and dark matter (green) in DMO simulations in a halo of mass  $7 \times 10^{14} M_\odot/h$ . The center is chosen to be at the potential minimum in the halo. The  $r$  range plotted is from the gravitational softening  $\epsilon = 1.85 \text{ kpc}/h$  up to  $2 \text{ Mpc}/h$ .

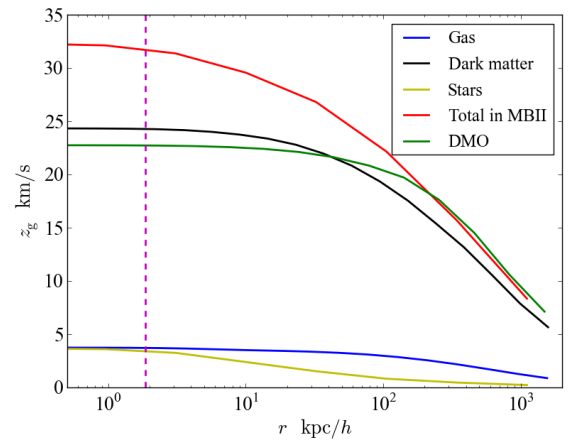


**Figure 3.** The gravitational redshift profiles of gas (blue), dark matter (black), stars (yellow) and total matter (red) in MBII and dark matter (green) in the DMO simulations in the halo of mass  $7 \times 10^{14} M_\odot/h$  in log-log space. The center is chosen at the potential minimum of the halo. The distance scale  $r$  spans the gravitational softening  $\epsilon = 1.85 \text{ kpc}/h$  to  $2 \text{ Mpc}/h$ .

increment in  $z_g$  in the centers for halos simulated with hydrodynamics relative to the DMO case. This size of this fractional increment depends on halo mass, and presence of substructures.

Fig. 4 shows the density distribution in the most massive halo as well as contours of gravitational redshift. The halo contains substantial substructure. The gravitational redshift contours are much smoother than the mass distribution.



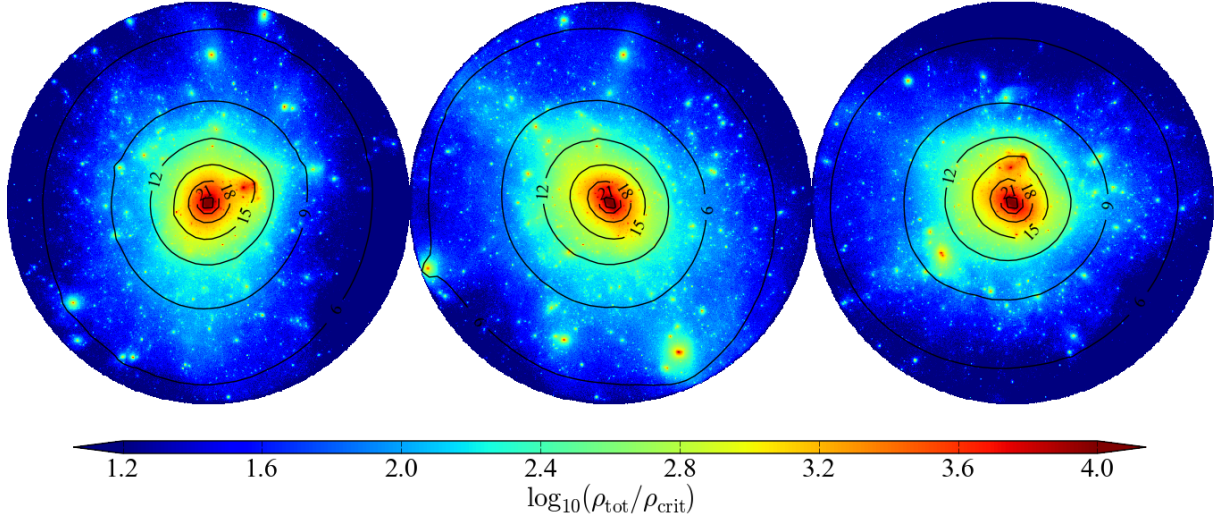


**Figure 4.** 2D plots showing the density of all types of particles (gas, dark matter, stars) in the MBII simulation in a slice of thickness  $\pm 400$  kpc/h diameter 4 Mpc/h centered on the gravitational potential minimum. We show 3 different orthogonal planes. The colormaps show the density and the contours represent the gravitational redshift. The subplots are the slices in the  $X-Y$ ,  $X-Z$  and  $Y-Z$  planes respectively from left to right.

### 3.2 Surface (projected) profiles

In order to relate our simulation results to quantities that are directly measurable from observations, we turn to projected profiles. We investigate the spatial (deprojected) and surface (projected) profiles of both the density and the gravitational redshift in Fig. 5. We also choose the center of our profiles to be the potential minimum of the halo. To estimate the density profiles, we accumulate the mass in each bin and divide it by the bin area or volume as appropriate ( $4\pi r^2 \Delta r/3$ ) for spherical bins and ( $2\pi R \Delta R$ ) for cylindrical bins; this leads to a difference in the units, (see Eqn. 4):

$$\rho_{k,\text{spatial}} = \frac{\sum_{r_i \geq r_k - \Delta r/2}^{< r_k + \Delta r/2} m_i}{4\pi [(r_k + \Delta r/2)^3 - (r_k - \Delta r/2)^3]}, \quad (4a)$$

$$\rho_{k,\text{projected}} = \frac{\sum_{R_i \geq R_k - \Delta R/2}^{< R_k + \Delta R/2} m_i}{2\pi [(R_k + \Delta R/2)^2 - (R_k - \Delta R/2)^2]}, \quad (4b)$$

where  $k$  indicate the radial bin number,  $m_i$  is the mass of the  $i$ -th particle.  $r_k$  and  $R_k$  are the distances to the center of the  $k$ -th bin and  $\Delta r$  and  $\Delta R$  are bin sizes.

To compute the gravitational redshift profiles we use the mass weighted gravitational redshift in spherical or cylindrical bins (see Eqn. 5):

$$z_{g,\text{spatial}} = \frac{\sum_{r_i \geq r_k - \Delta r/2}^{< r_k + \Delta r/2} z_i}{\sum_i I(r_k - \Delta r/2 \leq r_i < r_k + \Delta r/2)}, \quad (5a)$$

$$z_{g,\text{projected}} = \frac{\sum_{R_i \geq R_k - \Delta R/2}^{< R_k + \Delta R/2} z_i}{\sum_i I(R_k - \Delta R/2 \leq R_i < R_k + \Delta R/2)}, \quad (5b)$$

where  $I(\cdot)$  is an indicator function.

We find that for density profiles the surface profile is

much flatter than the spatial one while the trend is completely different for gravitational redshift profiles (projected being almost the same as spatial, and even slightly steeper). The reason for this is that spatial and surface density profiles are normalized by different bin sizes, thus the profile has different dependencies on  $r$  or  $R$ . In general, for quantities such as gravitational redshift, the surface profile  $F(R)$  can be derived from the spatial profile  $f(r)$  using Abel transform, see [Abel \(1826\)](#)

$$F(R) = 2 \int_R^\infty \frac{f(r) r dr}{\sqrt{r^2 - R^2}}, \quad (6)$$

where  $r$  and  $R$  are spatial and projected distance to the center respectively. We can learn from the above equation that the projected profile averages quantities along the line-of-sight so that more edge information is brought in. Thus, in the bottom panel of Fig. 5, the projected profile at  $R$  lies in between the spatial profile at  $r = R$  and the outskirts.

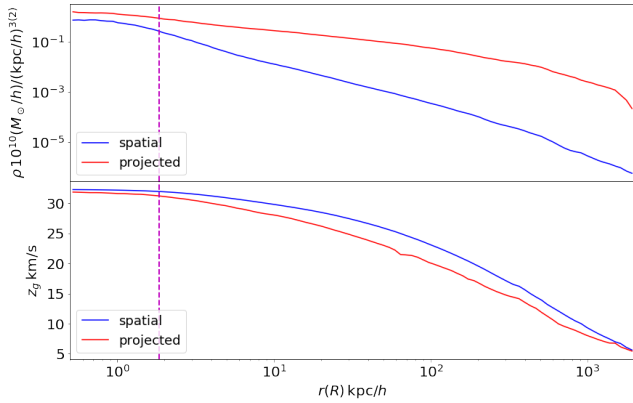


**Figure 5.** The density (top panel) and gravitational redshift (bottom panel) profiles of total matter in MBII in the halo of mass  $7 \times 10^{14} M_\odot/h$ . The center is chosen at the potential minimum. In each panel, the spatial (deprojected) profile is shown in blue while the surface (projected) profile is shown in red. The distance scale  $r$  spans the gravitational softening  $\epsilon = 1.85 \text{ kpc}/h$  to  $2 \text{ Mpc}/h$ .

#### 4 ANALYTIC MODELS OF DENSITY AND GRAVITATIONAL REDSHIFT PROFILES OF MASSIVE HALOS

As mentioned in Sec. 1, the dark matter density profile of a dark matter halo can be described by either NFW (See Eqn. 1), gNFW (See Eqn. 2) or Einasto (See Eqn. 3) models. The NFW profile is the simplest and the most commonly used dark matter profile. However, it is not able to control the slope of the inner profile, which is most affected by baryonic effects. Two other profiles, gNFW and Einasto are introduced to better model the dark matter halo and potentially can be used to describe the baryonic effects, by parametrizing the inner slope as  $d \ln \rho(r)/d \ln r|_{r \rightarrow 0} = -\gamma$  and  $d \ln \rho(r)/d \ln r = -2(r/r_{-2})^\alpha$  respectively. Gravitational redshift profiles can be calculated using these analytic density profiles.

For NFW density profiles, we need to assume an inner cut-off radius  $R_t$  to prevent logarithmic divergence.

$$\begin{aligned} \phi(r) &= -4\pi G \left[ \frac{1}{r} \int_0^r \rho(r) r^2 dr + \int_r^{R_t} \rho(r) r dr \right] \\ &= \frac{4\pi G \rho_{\text{crit}}(z) \delta_c r_s^3}{r_s + R_t} \left[ \frac{r_s + R_t}{r} \ln \left( \frac{r_s}{r + r_s} \right) + 1 \right] \\ &= \frac{4\pi G \rho_{\text{crit}}(z) \delta_c r_s^3}{r} \ln \left( \frac{r_s}{r + r_s} \right) + \phi_0. \end{aligned} \quad (7)$$

Since the second term of line 2 in Eqn. 7 is a constant, we can take only the first term and add a constant  $\phi_0$  to obtain line 3. As expected, the  $r$ -dependent term in line 3 is independent of  $R_t$ .

For gNFW density profiles,

$$\begin{aligned} \phi(r) &= \frac{4\pi G \rho_{\text{crit}}(z) \delta_c}{r^{\gamma-2}} \left[ \frac{r_s^\gamma {}_2F_1(3-\gamma, 3-\gamma; 4-\gamma; -r/r_s)}{\gamma-3} \right. \\ &\quad \left. + \frac{r_s^2 (r + r_s)^{\gamma-2}}{2-\gamma} \right] + \phi'_0, \end{aligned} \quad (8)$$

where  ${}_2F_1(a, b; c; z)$  is the hypergeometric function. The NFW density profile is therefore a special case of the gNFW density profile when  $\gamma = 1$ .

For Einasto density profiles, there is no analytic solution for the potential, and so we carry out the required integration numerically.

In order to apply these results to the gravitational potential profiles of halos in our simulations, we start by fitting the density profiles of the massive halos. Following Neto et al. (2007), we minimize the mean squared deviation between the binned data profile  $\rho$  and the model density profile  $\rho_{\text{model}}(\Theta)$  with a set of fitting parameters  $\Theta$  in log-log space, defined as

$$\sigma_{\text{density}}^2 = \frac{1}{N_b - 1} \sum_{i=1}^{N_b} (\log_{10} \rho_i - \log_{10} \rho_{\text{model},i}(\Theta))^2, \quad (9)$$

where  $N_b$  is the number of radial bins. Eqn. 9 is valid only when each bin has the same weight. We have also tried weighting each bin by the inverse variance due to Poisson noise but there is significant difference in our results. The parameter sets are  $\Theta = (\delta_c, r_s)$  for NFW density profiles,  $\Theta = (\delta_c, r_s, \gamma)$  for gNFW density profiles and  $\Theta = (\alpha, r_{-2}, \rho_{-2})$  for Einasto density profiles. After we fit the density profiles using the different models, we use the output parameters to calculate the  $z_g$  profiles. The evaluation of the goodness of fit for the  $z_g$  profiles is given by

$$\sigma_{\text{grav}}^2 = \frac{1}{N_b - 1} \sum_{i=1}^{N_b} (z_{g,i} - z_{g,\text{model},i}(\Theta))^2. \quad (10)$$

Dark matter halos, particularly of large mass are dynamic structures. Even though we might expect to see more relaxed halos at low redshift, Fig. 4 contains obvious substructure. Looking at all halos, irrespective of mass, there are cases among them where ongoing merging is obvious. It is therefore useful to quantify which halos are close to equilibrium states. Following Thomas et al. (2001) and Neto et al. (2007), we measure the degree of substructure based on the center of mass displacement, defining

$$s = \frac{|\mathbf{r}_c - \mathbf{r}_{\text{cm}}|}{R_{\text{vir}}}, \quad (11)$$

where  $\mathbf{r}_c$  denotes the potential minimum and  $\mathbf{r}_{\text{cm}}$  denotes the center of mass.  $s$  is referred to as the normalized offset. A *relaxed* halo requires  $s < 0.07$  to meet that definition. We have computed  $s$  for each of the ten most massive halos in the simulation and find one merger. We have eliminated it from Tbl. 2.

Fig. 6 shows density and gravitational redshift profiles of the most massive halo in the MBII catalogue as well as the corresponding mean squared errors on the fit ( $\sigma^2$ s). The two blocks of figures (each block has six panels) show fits to all types of particles in MBII, dark matter particles in MBII and DMO respectively. Looking at the left block first, we can see that the density fits from all three blocks (especially the bottom left panels in each block) demonstrate a consistent trend: the NFW profile is good in the outer regions but underestimates the density in the innermost regions. Not surprisingly, the NFW profile fits the DMO simulation the best, but both gNFW and Einasto density profiles do a better job as they have one more fit parameter. The right block also provides us with information on the influence of baryons. It is interesting to see that fitting parameters from the NFW relation applied to all types of particles in MBII (left panels on the right block) overestimate  $z_g$  near the center and

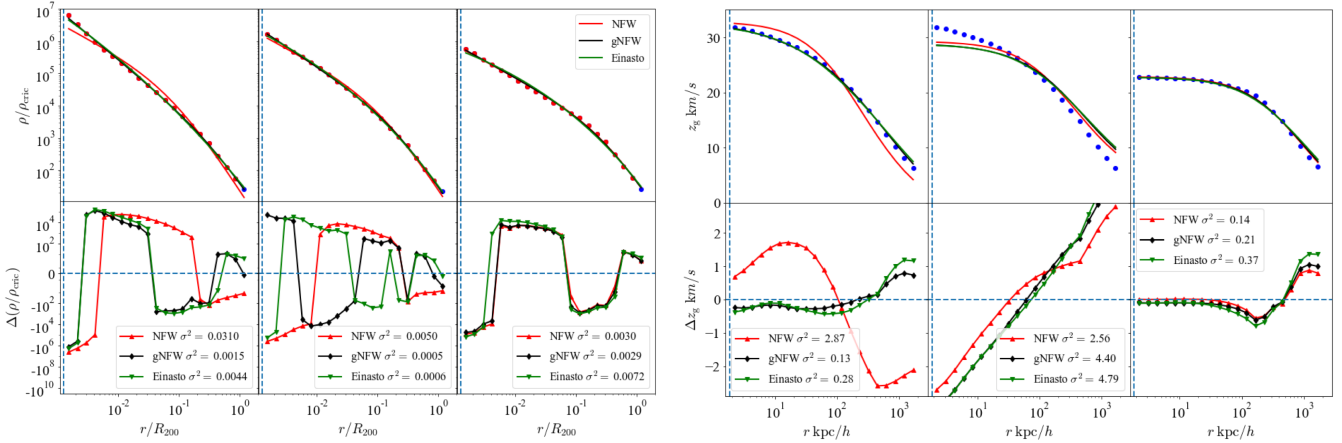


**Figure 6.** Halo density and gravitational redshift profiles for different types of particle and their analytic fits. The set of figures contains two blocks, from left to right, and each block contains six subplots. The left and right blocks illustrate fits to the density profiles and calculated gravitational redshift profiles measured from the particle data respectively. Inside each block, the top panels show fits to all types of particles in MBII (top left), dark matter particles in MBII (top middle), DMO (top right) and bottom panels show the differences between data and corresponding models. All plots are for the halo which in the MBII simulations has halo mass  $7 \times 10^{14} M_{\odot}/h$ . The center is chosen at the potential minimum in the halo. In the top right panel, the blue filled circles show the density profile of the halo. After taking into consideration the softening length,  $1.85 \text{ kpc}/h$ , data between  $2 \text{ kpc}/h$  and  $r_{200}$  (the red filled circles) are used in the fit.

underestimate  $z_g$  away from the center while they behave in quite the opposite fashion when applied to dark matter particles in MBII (middle panels on the right block). Among the three models, gNFW yields the best performance. We therefore propose that the most useful analytic gravitational redshift profile is the one based on the gNFW density profile, given by Eqn. 8.

So that the reader can reproduce the fit curves exactly, the parameters are listed in Tbl. 2 of the Appendix. We plot the concentration parameter  $\delta_c$  for all 9 halos in our study in Fig. 7. We can see that in each block, the most concentrated distribution is that of all types of particles in MBII while the least concentrated one is that of particles in DMO. This again shows that the effect of baryons is important in the inner regions, with the concentration increasing by almost an order of magnitude in some systems.

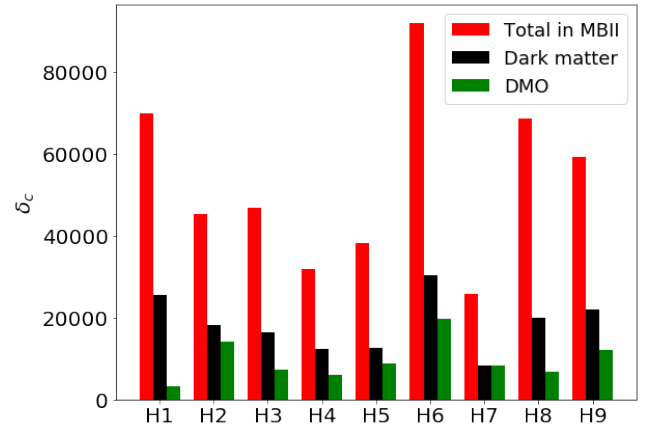


**Figure 7.** A bar plot showing the concentration  $\delta_c$  for the 9 most massive dynamically relaxed halos in the simulation. We give results for all particles (red), dark matter (black) in MBII and in dark matter-only simulations (green). Labels along  $x$ -axis indicate the different halos.

## 5 VELOCITIES AND THE TRANSVERSE DOPPLER EFFECT

In virialized objects such as dark matter halos, the gravitational redshift is supplemented by an additional component of comparable magnitude (Zhao et al. 2013). The observed wavelength of photons at redshift  $z$  is affected by the following relation,

$$\frac{c}{1+z} \frac{\lambda_{\text{obs}}}{\lambda_{\text{emit}}} = \left[ c + \frac{\phi - \mathbf{v}^2/2}{c} \right], \quad (12)$$

where  $\phi$  is the potential and  $\mathbf{v}$  is the peculiar velocity of the location from which the photon is emitted. The additional

velocity term is known as the Transverse Doppler (TD) effect, one of the main novel predictions of the Special Theory of Relativity related to object motion.

We have computed the TD effect profile in a similar fashion to the gravitational redshift profile, averaging the mass-weighted TD redshift in spherical cells centered on the center of each halo (chosen to be the minimum of the gravitational potential). Fig. 8 shows the TD profile of different components for the most massive halo. In general, the TD effect leads to a positive addition to the redshift, but with the outskirts being more redshifted than the halo center. This is opposite to the gravitational redshift, and therefore acts to suppress the overall redshift signal. The TD amplitude (difference between center and virial radius) is about 4 km/s, which is about 25% of the gravitational redshift. In detail, the TD effect increases with radius below 100 kpc/h and decreases with radius above 100 kpc/h.

This trend can be interpreted by assuming an isotropic power-law density distribution  $\rho \propto r^{-\alpha}$ . The enclosed mass is then  $M(r) = \int dr 4\pi r^2 \rho \propto r^{3-\alpha}$ . The tangential component of the velocity is therefore  $v_t = \sqrt{GM(r)/r} \propto r^{1-\alpha/2}$ , which leads to a TD effect profile  $v^2/2 = (3v_t)^2 \propto r^{2-\alpha}$ . This relation shows the TD effect is sensitive to the slope of the density profile. Referring to the blue curve in the left panel of Fig. 5,  $\alpha > 2$  when  $r$  is large, while  $\alpha$  becomes small when it comes closer to the core. This therefore qualitatively explains the transverse Doppler velocity profile shown in Fig. 8.

The different lines in Fig. 8 show the TD profiles measured from the different components in the MBII simulation, as well as the profile from the DMO simulation. In MBII, all components feel the same gravitational potential, and so one might expect the velocity dispersions, and hence the magnitude of the TD effect to be the same for all components. In fact, we see that the TD effect for the stars is approximately 50% smaller than for the dark matter in the central regions of the halo, and  $\sim 25\%$  lower around the virial radius. The red curve is the mass weighted average of all components and there is a  $\sim 10 - 15\%$  difference in TD between this and stars at the virial radius. This difference is related to the “velocity bias” that has been seen between galaxies and dark matter as tracers of the large-scale density field. [Armitage et al. \(2018\)](#) have found in galaxy clusters that mass estimates made from the velocity dispersion of stellar mass selected galaxies are only minimally affected by velocity bias (i.e., similar to estimates made using the dark matter velocities to within 5%). On the other hand, [Ye et al. \(2017\)](#) have shown how central galaxies in halos have a small (but still non negligible) velocity dispersion with respect to the dark matter.

In our case, because of the small numbers of subhalos in each halo, we have not computed the TD profiles after separating the mass in the different components into subhalos or galaxies. The possibility of differences in the TD effect between stars and dark matter should be borne in mind when comparing to observations, as should the effects of baryons overall. We do find, however that the effects of baryons on the TD effect are smaller than for the gravitational redshift. We can see this by comparing the stars curve (yellow) to the DMO profile (green). We see that on scales between  $\sim 2$ -10 kpc the stars are boosted by about 0.5 km/s in  $z_{\text{TD}}$ , which corresponds to a  $\sim 0.5$  km/s decrement in the overall red-

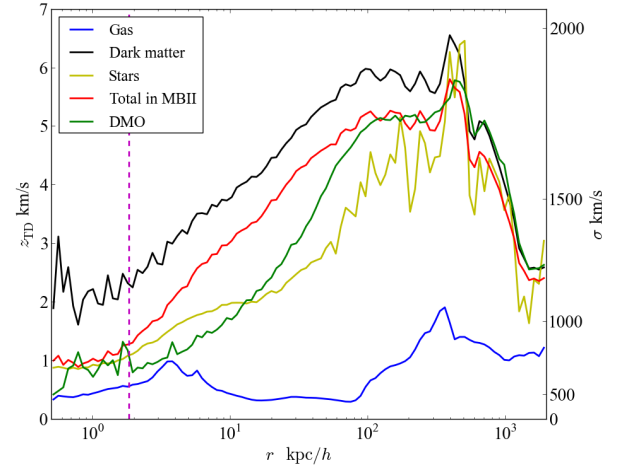


**Figure 8.** The transverse Doppler redshift profiles of gas (blue), dark matter (black), stars (yellow) and their average weighted by mass (red) in MBII and dark matter (green) in the DMO simulations. Results are for the halo of mass  $7 \times 10^{14} M_{\odot}/h$ . The center is chosen at the potential minimum of the halo. The distance  $r$  spans slightly above the gravitational softening  $\epsilon = 1.85$  kpc/h to 2 Mpc/h.

shift profile  $z_g$  (as  $z_{\text{TD}}$  has the opposite sign from Eqn. 12). On larger scales, up to the virial radius, the sign changes, but the effect is of similar magnitude.

## 6 CONCLUSIONS

We have explored the effects of baryons on the density, gravitational redshift and velocity profiles of the 9 most massive  $\Lambda$ CDM halos in the MBII hydrodynamical and dark matter-only (DMO) simulations. In the hydro run (MBII) we have studied the differences between dark matter profiles and all-particle profiles. We have also cross-compared dark matter profiles and all-particle profiles in MBII with the profiles from DMO. On large scales (several tens of kpc/h) we find good agreement among all three profiles (black, red and green lines in Fig. 2, Fig. 3 and Fig. 8, indicating that a reasonably good approximation to the profiles can be obtained using  $N$ -body simulations, as has been done in [Zhao et al. \(2013\)](#); [Cai et al. \(2017\)](#); [Zhu et al. \(2017\)](#).

On small scales we observe deviations from the  $N$ -body only simulations due to the clustering of baryons (gas and stellar particles). The baryons have excess concentration toward the center bringing dark matter particles inward, making the inner profile steeper than  $N$ -body simulations. This leads to a significant difference, an extra  $\sim 8$  km/s in gravitational redshift compared to the total 16 km/s difference between center and outskirts in  $N$ -body simulations of cluster sized halos. We fit density profiles with NFW, gNFW and Einasto relations to find quantitatively the differences for simulations with and without baryons. We find that baryons make density profiles 30%-50% more concentrated ( $c_{200}$ ).

We have examined the differences between projected redshift profiles (which can be measured more easily from observations) and spatial profiles. We find that projected



profiles, by including information from the edges of systems tend to resemble spatial profiles at larger radius. We have also studied the transverse Doppler effect which is expected to be a comparable effect in magnitude to the gravitational redshift. We find that baryonic effects are relatively small, at the  $\sim 0.5$  km/s level.

Overall, when considering the gravitational redshift profiles of galaxy clusters, such as those presented in Wojtak et al. (2011); Zhao et al. (2013); Bonvin et al. (2014); Zhu et al. (2017); Alam et al. (2017a); Giusarma et al. (2016); Cai et al. (2017), one should consider the possibility of baryonic and galaxy formation effects. These physical processes are those also relevant to mass determinations of galaxy clusters (Neto et al. 2007; Rudd et al. 2008; Duffy et al. 2010; Gnedin et al. 2011; Fedeli 2012; Velliscig et al. 2014; Chan et al. 2015; Schaller et al. 2015a,b).

We have learnt in the present work that baryonic effects are most important on small scales, in the centers of clusters. However, there are possible extensions to this work. For example, there are several other relativistic effects of the same order of magnitude which can affect the overall redshift profiles of clusters. These include the light cone effect and relativistic beaming effect mentioned by Kaiser (2013), Zhu et al. (2017), Alam et al. (2017b) and Breton et al. (2018). These effects are all potentially affected by the presence of baryons. In order to properly match the observations, one must consider a full model in which all these effects are taken into account. In addition, the mismatch between the hydrodynamic MBII simulation and the  $N$ -body only DMO run happens on galaxy scales, and on the scales of galaxy potentials. As measurements of gravitational redshifts are made using the differences between galaxy redshifts, simulations that explore the structure in galaxy potentials at higher resolution are also needed.

## ACKNOWLEDGMENTS

This work was supported by NSF Award AST-1412966. SA is also supported by the European Research Council through the COSFORM Research Grant (#670193). RACC would like to thank the Astrophysics group at the University of Melbourne for their hospitality and the support of a Lyle Fellowship. We thank Nishikanta Khandai and Ananth Tenneti for providing halo and subhalo catalogues of the MassiveBlack II and MassiveBlack II dark matter-only simulations.

## REFERENCES

Abel N., 1826, *Journal für die reine und angewandte Mathematik*, 1, 153  
 Alam S., Zhu H., Croft R. A. C., Ho S., Giusarma E., Schneider D. P., 2017a, *MNRAS*, 470, 2822  
 Alam S., Croft R. A. C., Ho S., Zhu H., Giusarma E., 2017b, *MNRAS*, 471, 2077  
 Armitage T. J., Barnes D. J., Kay S. T., Bahé Y. M., Dalla Vecchia C., Crain R. A., Theuns T., 2018, *MNRAS*, 474, 3746  
 Bonvin C., Hui L., Gaztañaga E., 2014, *Phys. Rev. D*, 89, 083535  
 Breton M.-A., Rasera Y., Taruya A., Lacombe O., Saga S., 2018, preprint, ([arXiv:1803.04294](https://arxiv.org/abs/1803.04294))  
 Cai Y.-C., Kaiser N., Cole S., Frenk C., 2017, *MNRAS*, 468, 1981

Cappi A., 1995, *A&A*, 301, 6  
 Chan T. K., Kereš D., Oñorbe J., Hopkins P. F., Muratov A. L., Faucher-Giguère C.-A., Quataert E., 2015, *MNRAS*, 454, 2981  
 Croft R. A. C., 2013, *MNRAS*, 434, 3008  
 Davis M., Efstathiou G., Frenk C. S., White S. D. M., 1985, *ApJ*, 292, 371  
 Dodelson S., 2003, *Modern cosmology*. Academic press  
 Duffy A. R., Schaye J., Kay S. T., Dalla Vecchia C., Battye R. A., Booth C. M., 2010, *MNRAS*, 405, 2161  
 Einasto J., 1965, *Trudy Astrofizicheskogo Instituta Alma-Ata*, 5, 87  
 Einstein A., 1916, *Annalen Der Physik*, 49, 770  
 Falcon R. E., Winget D. E., Montgomery M. H., Williams K. A., 2010, *ApJ*, 712, 585  
 Fedeli C., 2012, *MNRAS*, 424, 1244  
 Giusarma E., Alam S., Zhu H., Croft R. A. C., Ho S., 2016, xxx, pp xx–xx  
 Gnedin O. Y., Ceverino D., Gnedin N. Y., Klypin A. A., Kravtsov A. V., Levine R., Nagai D., Yepes G., 2011, preprint, ([arXiv:1108.5736](https://arxiv.org/abs/1108.5736))  
 Hernquist L., 1990, *ApJ*, 356, 359  
 Huang H.-J., Eifler T., Mandelbaum R., Dodelson S., 2018, preprint, ([arXiv:1809.01146](https://arxiv.org/abs/1809.01146))  
 Kaiser N., 2013, *MNRAS*, 435, 1278  
 Khandai N., Di Matteo T., Croft R., Wilkins S., Feng Y., Tucker E., DeGraf C., Liu M.-S., 2015, *MNRAS*, 450, 1349  
 Kim Y.-R., Croft R. A. C., 2004, *ApJ*, 607, 164  
 McDonald P., 2009, *J. Cosmology Astropart. Phys.*, 11, 026  
 Merritt D., Navarro J. F., Ludlow A., Jenkins A., 2005, *ApJ*, 624, L85  
 Merritt D., Graham A. W., Moore B., Diemand J., Terzić B., 2006, *AJ*, 132, 2685  
 Moore B., Quinn T., Governato F., Stadel J., Lake G., 1999, *MNRAS*, 310, 1147  
 Navarro J. F., Frenk C. S., White S. D. M., 1996, *ApJ*, 462, 563  
 Navarro J. F., Frenk C. S., White S. D. M., 1997, *ApJ*, 490, 493  
 Navarro J. F., et al., 2004, *MNRAS*, 349, 1039  
 Neto A. F., et al., 2007, *MNRAS*, 381, 1450  
 Pound R. V., Rebka G. A., 1959, *Physical Review Letters*, 3, 439  
 Rudd D. H., Zentner A. R., Kravtsov A. V., 2008, *ApJ*, 672, 19  
 Schaller M., et al., 2015a, *MNRAS*, 451, 1247  
 Schaller M., et al., 2015b, *MNRAS*, 452, 343  
 Schmidt R. W., Allen S. W., 2007, *MNRAS*, 379, 209  
 Sérsic J. L., 1963, *Boletín de la Asociacion Argentina de Astronomia La Plata Argentina*, 6, 41  
 Springel V., 2005, *MNRAS*, 364, 1105  
 Springel V., Yoshida N., White S. D. M., 2001, *New Astron.*, 6, 79  
 Takeda Y., Ueno S., 2012, *Sol. Phys.*, 281, 551  
 Tenneti A., Mandelbaum R., Di Matteo T., Kiessling A., Khandai N., 2015, *MNRAS*, 453, 469  
 Thomas P. A., Muanwong O., Pearce F. R., Couchman H. M. P., Edge A. C., Jenkins A., Onuora L., 2001, *MNRAS*, 324, 450  
 Velliscig M., van Daalen M. P., Schaye J., McCarthy I. G., Cacciato M., Le Brun A. M. C., Dalla Vecchia C., 2014, *MNRAS*, 442, 2641  
 Wojtak R., Hansen S. H., Hjorth J., 2011, *Nature*, 477, 567  
 Ye J.-N., Guo H., Zheng Z., Zehavi I., 2017, *ApJ*, 841, 45  
 Yoo J., Fitzpatrick A. L., Zaldarriaga M., 2009, *Phys. Rev. D*, 80, 083514  
 Yoo J., Hamaus N., Seljak U., Zaldarriaga M., 2012, *Phys. Rev. D*, 86, 063514  
 Zentner A. R., Semboloni E., Dodelson S., Eifler T., Krause E., Hearin A. P., 2013, *Phys. Rev. D*, 87, 043509  
 Zhao H., 1996, *MNRAS*, 278, 488  
 Zhao H., Peacock J. A., Li B., 2013, *Phys. Rev. D*, 88, 043013  
 Zhu H., Alam S., Croft R. A. C., Ho S., Giusarma E., 2017, *MNRAS*, 471, 2345

de Blok W. J. G., 2010, [Advances in Astronomy](#), 2010, 789293  
de Vaucouleurs G., 1948, *Annales d'Astrophysique*, 11, 247

## APPENDIX

**Table 2.** Outputs of the fitting parameters: Columns:  $M_{\text{group}}$  is the group mass.  $\delta_c$  and  $r_s$  are the outputs from 2-param NFW density profile.  $c_{200}$  and  $r_{200}$  are calculated from  $\delta_c$  and  $r_s$ .  $\alpha$ ,  $r_{-2}$  and  $\rho_{-2}/\rho_{\text{crit}}$  are the outputs from Einasto density profile. Rows: there are 9 blocks representing the top 10 massive halos excluding one merger. The first line of each block shows the (derived) fitting parameters with all types of particles, the second line shows the (derived) fitting parameters from dark matter particles and the third line shows the (derived) fitting parameters from DMO.

$M_{\text{group}} [10^{10} M_{\odot}/h]$	$r_{200} [\text{kpc}/h]$	$r_s [\text{kpc}/h]$	$c_{200}$	$\delta_c$	$\alpha$	$r_{-2} [\text{kpc}/h]$	$\rho_{-2}/\rho_{\text{crit}}$
$7.19 \times 10^4$	1431.6	119.5	11.98	$6.99 \times 10^4$	0.0816	262.2	$4.87 \times 10^{-5}$
$7.19 \times 10^4$	1431.6	180.1	7.95	$2.57 \times 10^4$	0.1488	264.7	$4.52 \times 10^{-5}$
$7.47 \times 10^4$	1449.2	448.3	3.23	$3.32 \times 10^3$	0.1764	549.9	$1.11 \times 10^{-5}$
$4.89 \times 10^4$	1258.4	125.2	10.05	$4.53 \times 10^4$	0.0388	1093.5	$1.17 \times 10^{-6}$
$4.89 \times 10^4$	1258.4	183.3	6.86	$1.81 \times 10^4$	0.1070	384.8	$8.47 \times 10^{-6}$
$5.0 \times 10^4$	1267.9	204.9	6.19	$1.42 \times 10^4$	0.1378	340.0	$1.38 \times 10^{-5}$
$3.66 \times 10^4$	1143.1	112.3	10.18	$4.68 \times 10^4$	0.1151	185.0	$6.58 \times 10^{-5}$
$3.66 \times 10^4$	1143.1	174.2	6.56	$1.63 \times 10^4$	0.1832	218.9	$4.41 \times 10^{-5}$
$3.73 \times 10^4$	1150.3	247.9	4.64	$7.34 \times 10^3$	0.2154	261.1	$3.66 \times 10^{-5}$
$3.09 \times 10^4$	1079.5	124.3	8.69	$3.18 \times 10^4$	0.1165	207.82	$3.59 \times 10^{-5}$
$3.09 \times 10^4$	1079.5	184.8	5.84	$1.24 \times 10^4$	0.1802	232.2	$2.67 \times 10^{-5}$
$3.11 \times 10^4$	1081.8	255.8	4.23	$5.96 \times 10^3$	0.1955	287.3	$1.96 \times 10^{-5}$
$2.69 \times 10^4$	1031.8	110.0	9.38	$3.83 \times 10^4$	0.0868	232.4	$2.78 \times 10^{-5}$
$2.69 \times 10^4$	1031.8	174.8	5.90	$1.27 \times 10^4$	0.1614	243.4	$2.43 \times 10^{-5}$
$2.99 \times 10^4$	1061.0	211.5	5.05	$8.89 \times 10^3$	0.1682	287.5	$1.99 \times 10^{-5}$
$2.58 \times 10^4$	1017.2	76.1	13.38	$9.19 \times 10^4$	0.0631	212.6	$2.66 \times 10^{-5}$
$2.58 \times 10^4$	1017.2	119.3	8.53	$3.03 \times 10^4$	0.1321	228.1	$2.20 \times 10^{-5}$
$2.79 \times 10^4$	1043.3	146.3	7.13	$1.98 \times 10^4$	0.1411	276.7	$1.73 \times 10^{-5}$
$2.48 \times 10^4$	1003.5	125.8	7.97	$2.59 \times 10^4$	0.1200	193.1	$4.11 \times 10^{-5}$
$2.48 \times 10^4$	1003.5	203.6	4.93	$8.41 \times 10^3$	0.2041	221.8	$3.03 \times 10^{-5}$
$2.55 \times 10^4$	1013.5	206.6	4.91	$8.32 \times 10^3$	0.1945	237.0	$3.00 \times 10^{-5}$
$1.91 \times 10^4$	919.7	77.3	11.91	$6.88 \times 10^4$	0.0422	165.1	$3.99 \times 10^{-5}$
$1.91 \times 10^4$	919.7	128.4	7.16	$2.00 \times 10^4$	0.1237	191.0	$2.98 \times 10^{-5}$
$1.93 \times 10^4$	922.7	207.1	4.46	$6.70 \times 10^3$	0.2017	224.1	$2.96 \times 10^{-5}$
$1.83 \times 10^4$	906.8	80.9	11.21	$5.93 \times 10^4$	0.0875	151.1	$4.82 \times 10^{-5}$
$1.83 \times 10^4$	906.8	121.6	7.46	$2.20 \times 10^4$	0.1535	186.9	$2.96 \times 10^{-5}$
$1.82 \times 10^4$	906.1	156.8	5.78	$1.21 \times 10^4$	0.1781	224.6	$2.41 \times 10^{-5}$